Optical Materials 101 (2020) 109739

Contents lists available at ScienceDirect

Optical Materials

journal homepage: http://www.elsevier.com/locate/optmat

Preparation of MgF_2/SiO_2 coating with broadband antireflective coating by using sol–gel combined with electron beam evaporation

Xiaoyu Sun, Xiaozhuang Xu, Guanyu Song, Jielei Tu *, Lei Li, Pinyuan Yan, Weinan Zhang, Kai Hu

Yunnan Key Laboratory of Rural Energy Engineering, Kunming, 650500, China

ARTICLE INFO

Keywords:
Antireflective coating
Multilayer coatings
Nanoporous SiO_2
MgF_2
Electron beam evaporation
Sol–gel

ABSTRACT

The broadband antireflective coatings (ARCs) can effectively reduce the optical loss in the transmittance process and improve energy efficiency in solar cells. MgF_2/SiO_2 bilayer films were prepared on the surface of soda–lime substrates via sol–gel spin-coating combined with electron beam (e-beam) evaporation. The bottom layer was the MgF_2 film obtained from e-beam evaporation, whereas the top layer was the nanoporous SiO_2 film via sol–gel spin-coating method. The refractive indices of MgF_2 and SiO_2 layers at 550 nm are 1.38 and 1.12, respectively. The structural, morphological, and optical properties of the films were characterized. The effects of annealing temperature, Triton X-100 concentration, and spin-coating speed on the properties of the film were investigated. The transmittance spectra of the coatings were investigated, and the broadband antireflective performance of the bilayer structure was examined. A bilayer coating with optical properties close to the theoretical design results was obtained by optimizing the refractive index and the thickness of the double coatings. The solar transmittances of the soda–lime glass coated with the MgF_2/SiO_2 bilayer antireflective film increased by 8.89% at 400–800 nm. The multilayer antireflective film exhibits promising applications in photoelectric devices, high power laser systems, and antidazzle glasses.

1. Introduction

Antireflective coating (ARC) is one of the most widely used and most productive optical films; it is used in daily life, industry, astronomy, military science, electronics, and other fields [1–6]. It is also an important component in photovoltaic (PV) systems and plays a key role in many fields. It can be prepared using several methods, such as electron beam (e-beam) evaporation, magnetron sputtering, chemical vapor deposition, and sol–gel process. Among these methods, sol–gel process is the most advantageous because of its high production speed, low cost, and simplicity, and it is essential to constitute coating with adjustable refractive index [7]. Minimum reflectance can be achieved by fine control of coating thickness and refractive index [8,9]. For monolayer ARC, near 100% transmittance can be reached given the following condition:

$$n_1 = (n_2 n_s)^{\frac{1}{2}} \quad (1)$$

where n_1, n_2 and n_s are refractive indexes of the coating, air and substrate, respectively [10]. ARC can be used to reduce the reflectivity of a solar panel, thereby increasing the solar cell's electrical performance.

Interest in studying ARC has been increasing in recent years. Several high transparent materials, such as SiO_2 (n = 1.44), SiO (n = 1.8–1.9), MgF_2 (n = 1.38), Si_3N_4 (n = 1.9), TiO_2 (n = 2.3), Al_2O_3 (n = 1.86), Ta_2O_5 (n = 2.26), SiO_2–TiO_2 (n = 1.8–1.96), ZnO (n = 1.34), and ZnS, have been used in the ARC field [11–20]. Ye et al. prepared a hydrophobic single layer SiO_2 ARC via the sol–gel process [21]. Chen used the sol–gel process to prepare ZnO nanorod arrays as an ARC and studied the effects of growth time, spin-coating rates, and solution concentration [22]. For a long time, sol–gel process has been used to obtain a series of films with a wide range of optical properties. Many reports on the preparation of nanoporous silicon coatings by sol–gel process are accessible [23–32]. However, most studies about ARC have only focused on the preparation of a monolayer. Monolayer coating has many limitations. According to Fresnel reflection theory, monolayer ARC can only be limited to one wavelength of antireflective performance [33,34], whereas multilayer ARC have good wide-spectrum antireflective performance [35–37]. Among the several parameters of the bilayer antireflective coatings (ARCs), the refractive index of the top layer is a sensitive parameter.

* Corresponding author.
E-mail address: tjl@ynnu.edu.cn (J. Tu).

https://doi.org/10.1016/j.optmat.2020.109739
Received 16 November 2019; Received in revised form 29 January 2020; Accepted 4 February 2020
Available online 13 February 2020

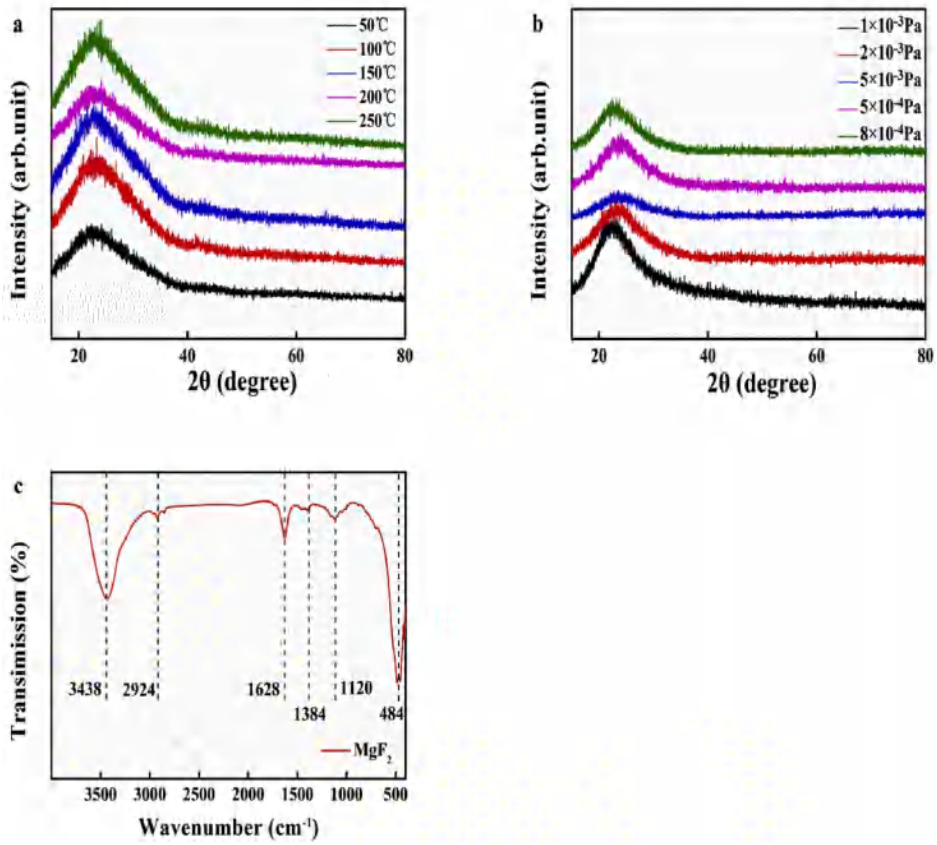

Fig. 1. (a–b) XRD images of MgF_2 coatings prepared at different substrate temperatures and vacuum degrees and (c) FT-IR Spectra of MgF_2 coating.

Hence, low refractive index allows researchers to easily design an ARC with a broad band.

In this study, MgF_2/SiO_2 bilayer ARC with broadband antireflective performance over the solar spectrum was prepared via sol–gel process combined with e-beam evaporation. The bilayer coatings consist of an MgF_2 bottom-layer and a nanoporous SiO_2 top-layer. MgF_2 and SiO_2 films were prepared on the surface of soda–lime glass substrates via e-beam evaporation and sol–gel spin-coating, respectively. The refractive index of SiO_2 coating can be adjusted from 1.12 to 1.28 due to its nanoporous structure. On the basis of the parameters of bilayer broadband ARCs designed by multilayer theory, MgF_2/SiO_2 bilayer ARCs with properties similar to the theoretical optical properties were prepared by optimizing the parameter. The structural, annealing temperature, morphological, and optical properties of the monolayer and the bilayer coatings were investigated.

2. Experimental details

2.1. Materials

Absolute ethanol (EtOH, 99.9%), tetraethylorthosilicate (TEOS, 99%), and hydrochloric acid (HCl, 37%) were purchased from Tianjin Kemiou Chemical Reagents Co., Ltd. (Tianjin, China). Ammonia–water (25%–28%), Triton X-100 (TX-100, 98%), and acetone were obtained from Aladdin (Shanghai, China). The water was deionized.

2.2. Cleaning substrate

To allow the film to adhere to the substrate steadily, the substrates were ultrasonically cleaned with deionized water, acetone, and hydrochloric acid (pH = 1) separately for 15 min. Finally, the soda–lime glass substrates were placed in ethanol for storage. They are taken out and dried in a dry air atmosphere at 70 °C prior to coating.

2.3. Preparation of monolayer MgF_2 coating

MgF_2 film was prepared on the soda–lime glass substrates using the e-beam evaporation coating system ZHD-500 (Beijing tycoon technology Co., Ltd, China). The evaporation material was MgF_2 particles with a purity of 99.99%. The soda–lime glass (Size: 20 × 20 × 1.5 mm) substrates were washed prior to deposition. These substrates were used for the deposition of MgF_2 thin films. In addition, fresh MgF_2 particles were used for every experiment. During the deposition, the pressure of the chamber was maintained at 1×10^{-3}, 2×10^{-3}, 5×10^{-3}, 1×10^{-4}, and 8×10^{-4} Pa and heated at temperatures of 50 °C, 100 °C, 150 °C, 200 °C, and 250 °C, respectively. The substrates were rotated at 25 revolutions per minute. The MgF_2 particles were placed in a graphite crucible. The distance between the crucible and substrate was about 27 cm. The thickness and deposition rate of the coatings were monitored using the silver aluminum crystal monitor. The deposition rate was controlled at 0.8–1.0 Å/s, and the monitored thickness was about 104 nm. Finally, the obtained films were annealed at 300 °C for 2 h.

2.4. Preparation of monolayer nanoporous SiO_2 coating

The initial silica sol was prepared based on the procedure used by Stöber et al. [38]. After being aged for 24 h, TX-100 was added to the solution, so that the TX-100 concentration reached 0, 0.15, 0.19, 5, 10, 15, 20, 25, 30, 35, 40, 45, and 50 g/L, respectively. The liquor was stirred for 1 h SiO_2 coating was then spin-coated on soda–lime glass substrates at 3000–9000 r min^{-1} for 30 s to investigate the effect of speed on film thickness. The film was treated at various annealing temperatures of 200 °C, 300 °C, and 400 °C for 2 h (h) in muffle furnace to investigate the effect of annealing temperature.

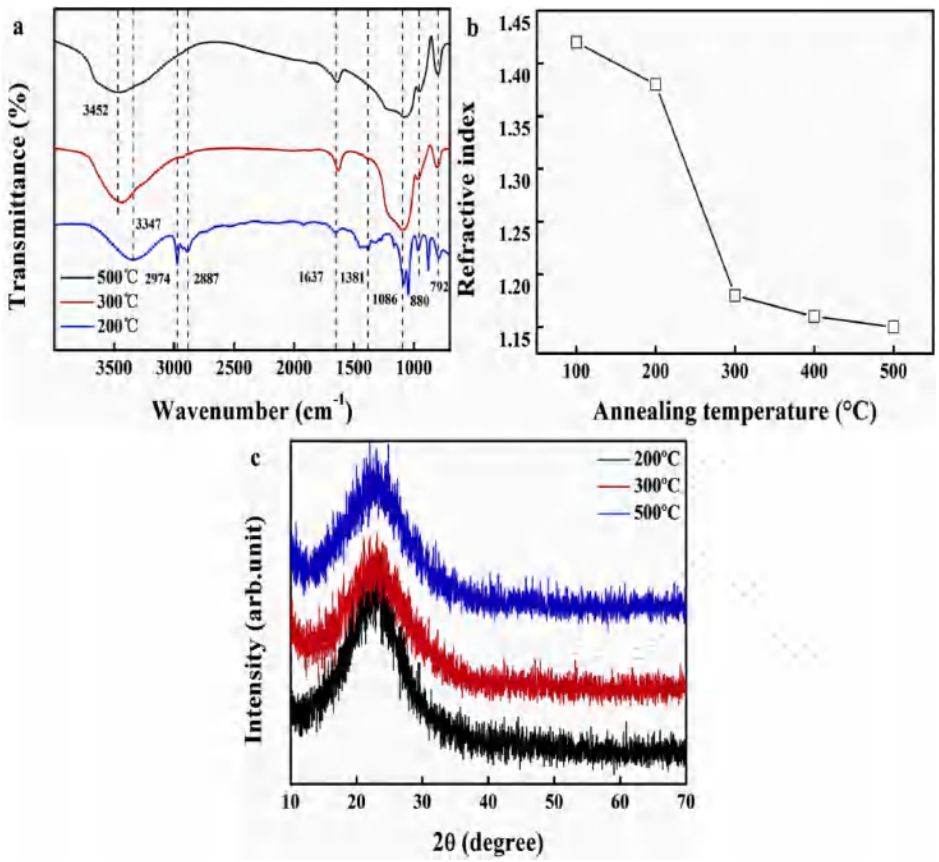

Fig. 2. (a–c) FT-IR spectrum, refractive index, and XRD image of the SiO_2 coating prepared with different annealing temperatures.

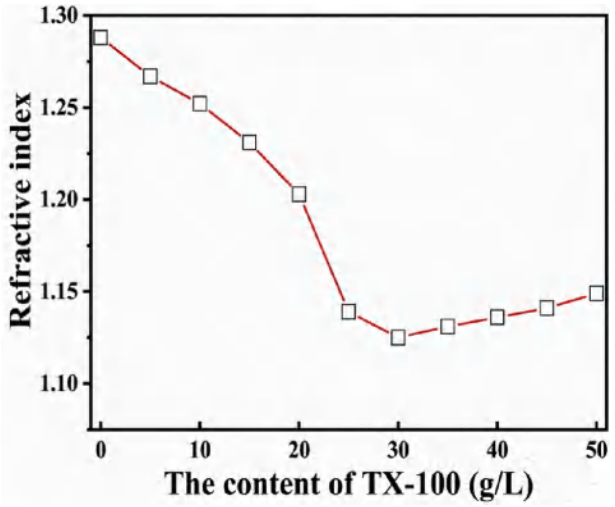

Fig. 3. Dependence of refractive index of the coatings on the TX-100 concentration prepared at sol's aging time of 3 days.

2.5. Preparation of bilayer ARC

The bilayer ARC was prepared via e-beam evaporation and sol–gel. The soda–lime glass (20 mm × 20 mm × 1.5 mm) was used as substrate, and the cleaning treatment was conducted following the steps in Section 2.20. Before the bilayer coating is prepared, the parameters of the bilayer ARC were simulated by simulation software to obtain the optimal parameters. ZHD-500 E-beam evaporator was used to place a monolayer MgF_2 coating on the soda–lime glass substrate. During the deposition process, the pressure of chamber was maintained at 8×10^{-4}Pa. The substrate is heated to 300 °C and was rotated at 25 revolutions per minute. The thickness and deposition rate of the films were monitored by quartz crystal monitor. The deposition rate was controlled at 0.8–1.0 Å/s and the monitored thickness was about 104 nm. The concentration of TX-100, spin-coating speeds and annealing temperature can be controlled to obtain the required refractive index and thickness. By studying the influence of various factors, the optimal spin-coating rate, annealing temperature and TX-100 concentration were 5000 r min^{-1}, 300 °C and 30 g/L, respectively. An optimized process can be used to obtain a SiO_2 coating with a refractive index of 1.12 and a thickness of 122 nm, which is well matched with the MgF_2 coating prepared by electron beam evaporation. After drying the MgF_2 coating at 80 °C for 30 min and heat treated at 300 °C for 2 h, a one-layer SiO_2 coating was prepared at 5000 r min^{-1} using a KW-4A spin coater. After being dried in an oven at 300 °C for 2 h and cooled to room temperature, MgF_2/SiO_2 bilayer broadband ARC could be obtained.

2.6. Characterization

The surface and cross-sectional micromorphology of the films were characterized using a field emission scanning electron microscope (FESEM, SEM450, Thermo). The energy dispersive x-ray (EDX) spectroscopy of film was recorded using a FESEM, SIGMA300, Zeiss). Fourier transform infrared (FT-IR) spectra were measured on a Nicolet iS10 FT-IR spectrometer using KBr pellets of the solid samples to study the chemical structure of the coatings. The crystal structure of the coating was observed by x-ray diffractometer (XRD, TTRIII, Rigaku). The transmittance spectrum of the glass covering the ARC in the range of 380–1400 nm was recorded by an ultraviolet visible spectrometer (UV-3600, SHIMADZU). The transmittance relative measurement errors are known to be within ±0.3%. The refractive index and film thickness were

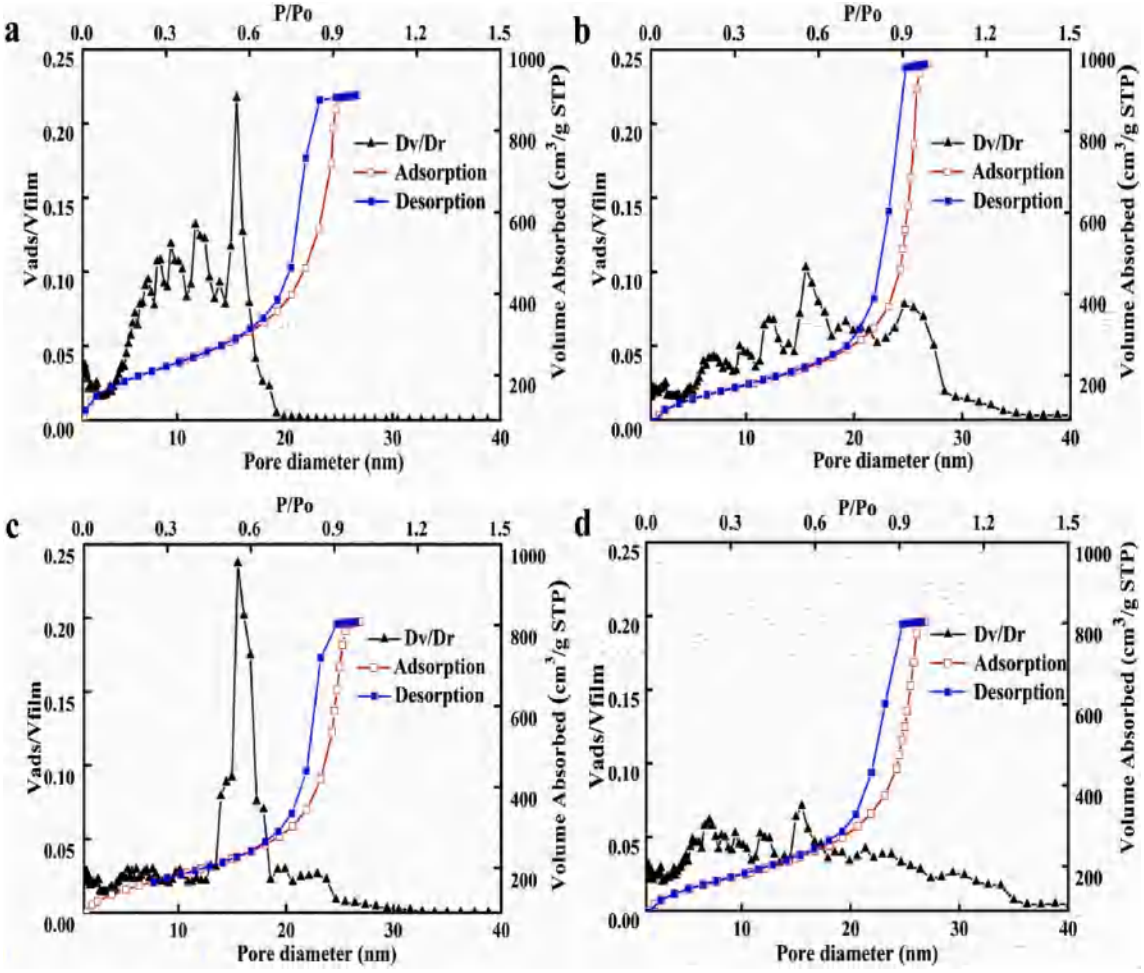

Fig. 4. Pore size distribution of TX-100 with the following concentrations: (a) 0 g/L, (b) 10 g/L, (c) 30 g/L, (d) 50 g/L.

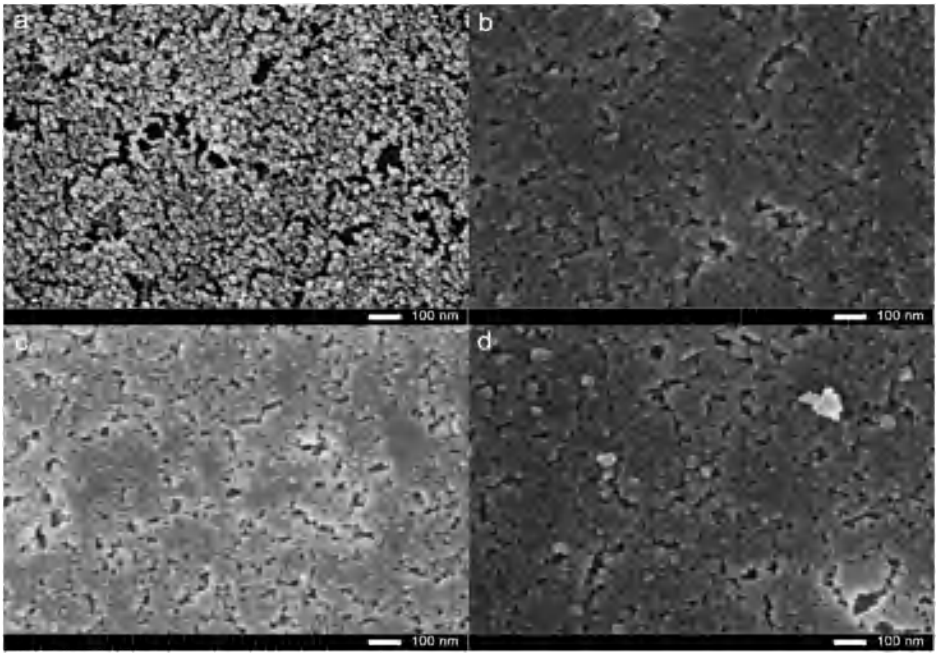

Fig. 5. FESEM image of TX-100 with the following concentrations: (a) 0 g/L, (b) 10 g/L, (c) 30 g/L, (d) 50 g/L.

Table 1
Refractive index of bilayer broadband ARCs on soda–lime glass substrates and their average transmittances were modeled by TFCalc in the range of 400–800 nm.

Sample number	Bottom layer		Top layer		Average transmittance (400–800 nm)%
	n_1	thickness [nm]	n_2	thickness [nm]	
1	1.38	104	1.12	122	99.89
2	1.38	99	1.12	164	99.52
3	1.38	120	1.12	164	99.46
4	1.38	150	1.12	134	99.41
5	1.38	88	1.13	104	99.85
6	1.38	108	1.13	142	99.81
7	1.38	121	1.13	151	99.64
8	1.38	150	1.13	132	99.46
9	1.38	104	1.14	115	99.92
10	1.38	104	1.14	156	99.62
11	1.38	121	1.14	149	99.66
12	1.38	104	1.15	149	99.71
13	1.38	85	1.15	110	99.88

measured by a spectroscopic ellipsometry (SENTECH SE800PV). Nitrogen adsorption–desorption measurements at 77K using Quadrasorb-evo were performed to obtain pore size distributions.

3. Results and discussion

The structure of the material has a crucial impact on performance. The XRD results of the MgF_2 films prepared using the e-beam method at different substrate temperatures and vacuum degrees are shown in Fig. 1 (a) and (b), respectively.

Fig. 1(a) and (b) do not show any sharp diffraction peaks. On this basis, the structure of the prepared magnesium fluoride film was amorphous. The FT-IR spectrum of MgF_2 film prepared via e-beam evaporation is shown in Fig. 1(c). The samples showed two absorption bands at 3438 and 1628 cm^{-1}, corresponding to telescopic and angular vibrations of −OH bond, respectively. The −OH bond on the surface of the coating was related to the adsorption of H_2O in the air. The formation of the MgF_2 coating was confirmed by absorption peaks of 1924, 1384, 1120, and 484 cm^{-1} in FT-IR spectra [39]. Therefore, the MgF_2 film prepared by the vacuum degree (8×10^{-4}-1×10^{-3} Pa) and substrate temperature (50 °C-250 °C) process has an amorphous structure.

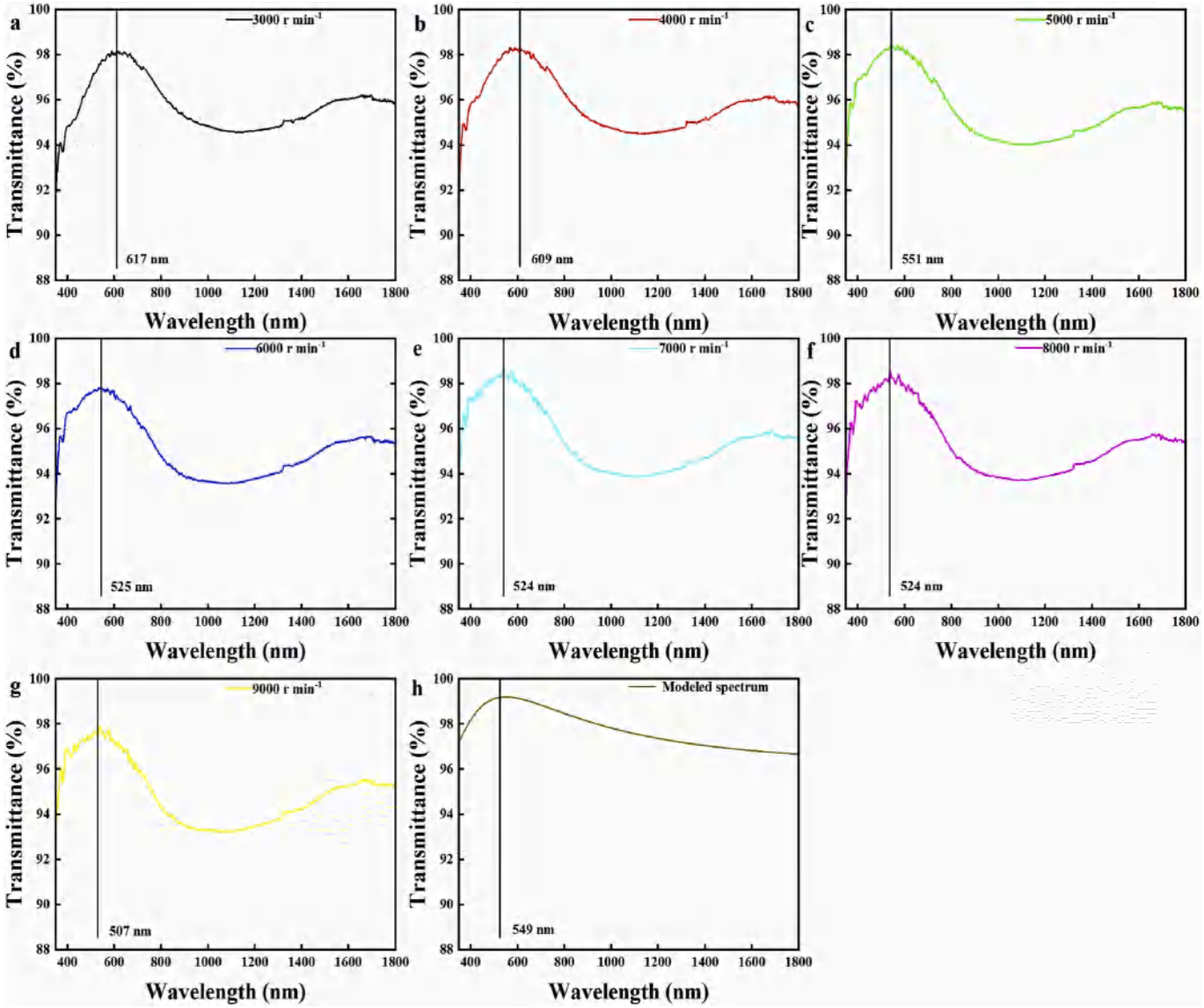

Fig. 6. (a–g) Transmission spectra and wavelength of maximum transmittance of SiO_2 coatings were prepared at different spin-coating speeds and (h) the target design transmittance spectra.

Table 2
Coating thickness was obtained at different spin-coating speeds.

Spin-coating speed (r min^{-1})	3000 r min^{-1}	4000 r min^{-1}	5000 r min^{-1}	6000 r min^{-1}	7000 r min^{-1}	8000 r min^{-1}	9000 r min^{-1}
Coating thickness (nm)	137	135	123	117	116	116	113

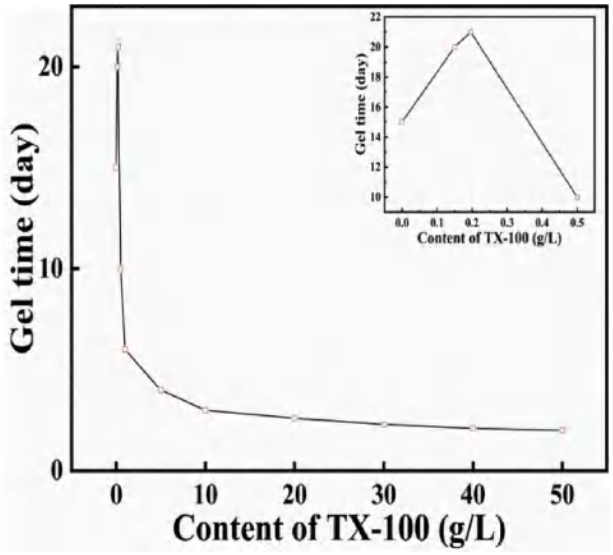

Fig. 7. Gel time of solutions with different concentrations of TX-100.

To study the effect of annealing temperature on silica gel, FT-IR spectra of silica sols with annealing temperatures of 200, 300, and 500 °C were obtained. As shown in Fig. 2, the absorption bands at 1086 and 792 cm^{-1}, corresponding to the stretching vibration of Si–O–Si bond [40]. The absorption peaks at 3452, 3347, and 1637 cm^{-1} attributed to −OH and H–O–H bending vibrations, which were caused by the adsorption of H_2O in the air [41]. For samples with an annealing temperature of 200 °C, two absorption peaks emerged at 2887 and 880 cm^{-1}, corresponding to the C–H stretching and bending vibrations, respectively. In addition, the absorption peaks of 2974 and 1381 cm^{-1} were caused by the stretching vibration of $-CH_3$ and the vibration of the C═C bond [42]. Hence, the TX-100 surfactant was removed at an annealing temperature of 300 °C. This result is consistent with the FT-IR analysis. The dependence of the refractive index on the annealing temperature is shown in Fig. 2(b). TX-100 concentration of the coating in Fig. 2 was 30 g/L. The refractive index value decreased steeply with the increase in temperature from 100 °C to 500 °C. This phenomenon may be related to the removal of surfactant TX-100. When TX-100 was incompletely removed, the refractive index of the film was high due to the high refractive index of TX-100 (n = 1.491). When TX-100 was completely removed, the refractive index dropped sharply. In addition, as shown in Fig. 2(c), the SiO_2 film had an amorphous structure according to the XRD images.

The measurement results of the refractive index of SiO_2 coatings with different TX-100 contents are shown in Fig. 3. The refractive index of the sample with TX-100 concentration of 0, 5, 10, 15, 20, 25, 30, 35, 40, 45, and 50 g/L was recorded. When the TX-100 content increased from 0 to 50 g/L, the refractive index curve of the coating showed a trend from decline to rise and reached the minimum at 30 g/L. Depending on the proportion of the TX-100, a series of coatings with different refractive indexes could be obtained. The addition and removal of TX-100 resulted in the formation of porous silica with ordered channels, as shown in Fig. 5. In addition, as shown in Fig. 4, the sample with a TX-100 concentration of 30 g/L had a relatively uniform pore size (15–20 nm) compared with other samples. The change in porosity in the coating was the main cause of the change in the refractive index of the coating. Normally, the relationship between refractive index and porosity can be obtained by the following equation [43]:

$$n_p = (n^2 - 1)(1 - p) + 1 \tag{2}$$

where n_p represents the refractive index of the porous coating; n represents the refractive index of the dense coating; and p represents the porosity of the coating.

When the concentration of TX-100 was less than 30 g/L, the surfactant could not be fully adsorbed on the surface of the silica sol. The thickness of the electric double layer increased slightly as well. Moreover, the van der Waals attraction was greater than the electrostatic repulsion force, and the probability of collision between particles increased. Therefore, the agglomeration of the particles was set to occur, and porosity is decreased. However, when the concentration of TX-100 in the solution was more than 30 g/L, excessive excess of the surfactant prevented the free movement of the particles and agglomeration occurs between the particles. ARC with different refractive indices were obtained by changing the ratio of TX-100. This method could be used to prepare ARCs with adjustable refractive index ranging from 1.12 to 1.28. The coating had a low refractive index and nanoporous structure, which could form a broadband ARC with other coatings due to the addition of TX-100 as a surfactant.

The refractive index of the top and bottom layers significantly affected the average transmittance of the bilayer ARCs. Following optical coating theory, the transmittance of the multilayer film could be calculated using the admittance feature matrix method. The characteristic matrix of the film system is given by Ref. [44].

$$\begin{bmatrix} B \\ C \end{bmatrix} = \prod_{j=1}^{k} \begin{bmatrix} \cos\delta_j & (i/\eta_j)\sin\delta_j \\ i\eta_j \sin\delta_j & \cos\delta_j \end{bmatrix} \begin{bmatrix} 1 \\ \eta_s \end{bmatrix} \tag{3}$$

where j, k, and l is the serial numbers of the bottom layer and top layer in contact with air, respectively, $\begin{bmatrix} B \\ C \end{bmatrix}$ is the characteristic matrix of the substrate and film combination; η_j is the optical correction admittance of layer j, δ_j is the phase thickness of layer j, and η_s is the optical correction admittance of substrate. In the case of normal incidence, is equal to (Refractive index of the Jth film) and is equal to n_{k+1}(Refractive index of the substrate). $\begin{bmatrix} \cos\delta_j & (i/\eta_j)\sin\delta_j \\ i\eta_j \sin\delta_j & \cos\delta_j \end{bmatrix}$ is the characteristic matrix of the Jth film [45]. $Y = C/B$ is a combination admittance of a multilayer film and a substrate. Therefore the reflectivity is given by

$$R = \left(\frac{\eta_0 B - C}{\eta_0 B + C}\right)\left(\frac{\eta_0 B - C}{\eta_0 B + C}\right)^{*} \tag{4}$$

where η_0 is the admittance of the incident medium. The η_0 of the incident medium is equal to n_0 because the incident medium is air [46].

Computer-aided design was chosen because it is fast and straightforward [47]. Consequently, a series of the bilayer broadband ARCs could be obtained by the above formula and the corresponding thin film design software (TFCalc). The optical properties of these ARCs with different parameters were modeled by TFCalc and are shown in Table 1. The refractive index of the bottom layer was set around 1.38, and it was fixed because it was prepared by electron beam evaporation. As shown in Table 1, the maximum transmittance was obtained when the refractive index of the top layer was set to 1.12. Meanwhile, the maximum theoretical average transmittance of 99.89% in the range of 400–800 nm can be calculated using TFCalc, when the thickness of the bottom and

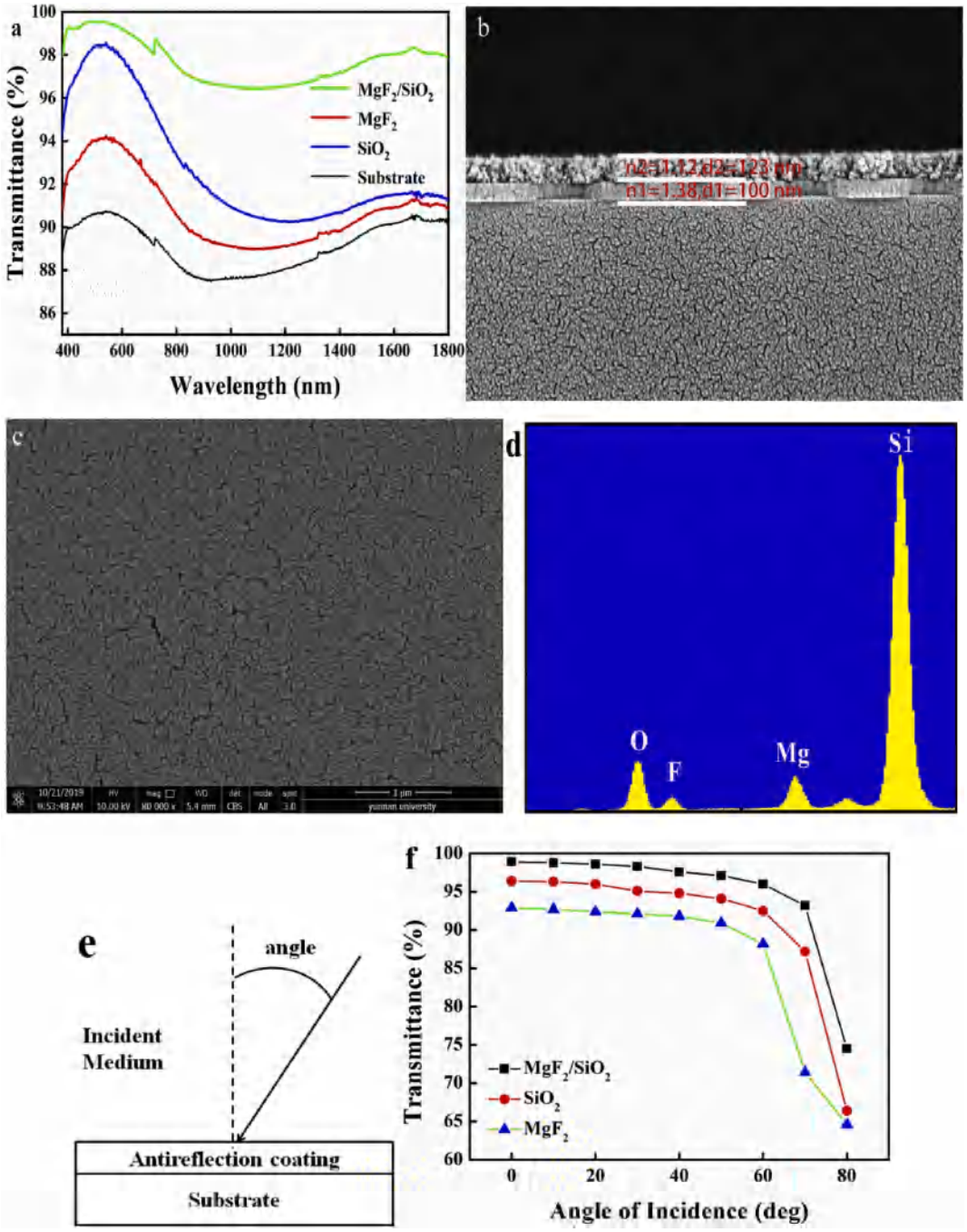

Fig. 8. (a) Experimental transmittance curves of MgF_2/SiO_2 bilayer broadband ARCs and the single SiO_2 and MgF_2 coating transmittance curves, (b) FESEM cross section images of the MgF_2/SiO_2 coating, (c) Surface view FESEM images of the MgF_2/SiO_2 coating, and (d) EDX spectrum of MgF_2/SiO_2 film, (e) Schematic diagram of incident angle, (f) MgF_2/SiO_2 bilayer broadband ARCs and the single SiO_2 and MgF_2 coating average transmittance at the incident angles of 0–80°.

top coatings was 104 and 122 nm, respectively (Sample 1).

The spin-coating speed was optimized to reach the parameters close to the top layer in sample 1. Generally, the thickness of the coating decreased with an increase in spin-coating speed when the viscosity was the same. As shown in Table 1, the thickness of coating heavily affected the average transmittance. Therefore, the thickness of the film in the experiment should be controlled [48]. The spin-coating speeds in the experiment were 3000, 4000, 5000, 6000, 7000, 8000, and 9000 r min^{-1}.

The thickness of the film could be accurately controlled by the spin-coating speed. By optimizing spin-coating speed, a bilayer ARC close to the theoretical thickness was obtained. We measured the transmission spectrum of SiO_2 film with TX-100 concentration of 30 g/L and refractive index of 1.14 at different spin-coating speeds in Fig. 6. As shown in the images, the maximum transmittance peak of the film moved to the left as the spin-coating speed increased. Film thickness can be obtained by

$$d = \frac{\lambda_0}{4n_1} \tag{5}$$

where λ_0 is the wavelength at the maximum transmittance; n_1 is the refractive index of the coating; and d is the thickness of the coating [49, 50]. The thickness corresponding to different spin-coating speeds via Equation (5) is shown in Table 2. Evidently, the film thickness was 123

nm when the spin-coating speed was 5000 r min^{-1} and the difference between the experimental and the target design wavelength of maximum transmittance is very little. Hence, 5000 r min^{-1} was chosen as the best speed in the experiment.

Gel time has important implications for large-scale industrial applications [51]. The gel time of the sols with TX-100 concentrations of 0, 0.15, 0.19, 0.5, 5, 10, 20, 30, 40, and 50 g/L were obtained. As shown in Fig. 7, when the concentration of TX-100 was greater than 0.19 g/L, the stability of the sol decreased as the concentration of TX-100 increased. Hence, the stability of the sol was controlled by many factors. Following Deijaguin-Landau and VerweyOverbeek (DLVO) theory, the stable existence of the sol depended on the magnitude of the opposite forces of the electric double layer repulsive force and the van der Waals attraction between the sol particles. When the sol particle distance (H) or the charging property changed to change the interparticle force (ET), the interaction force was converted into an attractive force by the absorption force, thereby causing the coagulation of particles. When the surfactant TX-100 concentration was less than 0.19 g/L, TX-100 increased the thickness of the electric double layer due to the adsorption on the surface of the silica sol, thereby further increasing the electrostatic adsorption force between the sol particles and stabilizing the system. When the concentration of surfactant TX-100 was greater than 0.19 g/L, the addition of TX-100 caused the viscosity of the solution to rise significantly. As a result, the sol particles made contact with one another under the action of H^+ and OH^- to polymerize. The reticular gel structure was finally formed.

The transmittance spectra of single SiO_2, MgF_2, and the bilayer broadband ARCs are shown in Fig. 8(a). As shown in Fig. 8(b), the cross sections of the MgF_2/SiO_2 bilayer ARCs were clearly defined. The thickness of the nanoporous SiO_2 coating with TX-100 concentration of 30 g/L was 123 nm, and the refractive index was 1.12. The thickness of the MgF_2 coating was 100 nm, and the refractive index was 1.38. The morphology of MgF_2/SiO_2 bilayer ARC at 300 °C was examined by FESEM, as shown in Fig. 8(c). The surface of the coating exhibited a nanoporous structure. To investigate the elemental composition, the EDX spectroscopy of MgF_2/SiO_2 thin film on soda–lime glass was conducted, as shown in Fig. 8(d). Strong silicon, oxygen, magnesium, and fluorine were recorded in the EDX spectrum of MgF_2/SiO_2 thin film. This observation clearly deduced the existence of Si, O, Mg, and F elements in the prepared ARC. Meanwhile, Optical theoretical calculations and many reports show that the angle of incidence can significantly affect the antireflection performance of the coating [52–55]. Therefore, the average transmittances at the incident angles of 0°, 10°, 20°, 30°, 40°, 50°, 60°,70°, and 80° of the different coating at a wavelength range of 400–800 nm can be obtained using spectrophotometer in Fig. 8(f). The schematic diagram of the incident angle is shown in Fig. 8(e). The results show that as the incident angle increases, the average transmittance decreases at the wavelength range of 400–800 nm. Moreover, compared to the monolayer coatings of MgF_2 and SiO_2, the MgF_2/SiO_2 bilayer antireflection film has better wide-angle antireflection performance.

The MgF_2/SiO_2 bilayer ARC exhibited excellent optical performance. The average experimental transmittance of the bilayer ARCs in the range of 400–800 nm was 98.89% using spectrophotometry. The transmittance relative measurement errors are known to be within ±0.3%. The results show that the experimental transmittance of the coated substrate is in good agreement with theoretical results at the wavelength range of 400–800 nm and the difference between the experimental (98.89%) and theoretical (99.89%) average transmittance is very small. After annealing of MgF_2, MgO was produced to increase the refractive index. Hence, the transmittance spectrum was different from the theoretical value.

4. Conclusions

In summary, the MgF_2/SiO_2 bilayer broadband ARCs with nanoporous structure were prepared on the surface of soda–lime glass substrates via sol–gel spin-coating process combined with e-beam evaporation. The structural, morphological, and optical properties of films were fully investigated. On the basis of the designed parameters of the bilayer ARCs and by the TFCalc optimization, the average transmittance of bilayer ARCs reached 98.89% in the range of 400–800 nm, where the bottom layer was a MgF_2 coating with the refractive index being 1.38 and the thickness was 100 nm. The top layer was a nanoporous SiO_2 coating with a refractive index of 1.12 and a thickness of 123 nm. The MgF_2/SiO_2 bilayer coatings showed excellent optical property. Therefore, the MgF_2/SiO_2 film can be used in many fields, such as optical devices and solar glass covers.

Declaration of competing interest

The authors declare that they have no known competing interests or personal relationships that could have appeared to influence the work reported in this paper.

CRediT authorship contribution statement

Xiaoyu Sun: Conceptualization, Methodology, Software, Investigation, Writing - original draft. **Xiaozhuang Xu:** Validation, Formal analysis, Visualization, Software. **Guanyu Song:** Validation, Formal analysis, Visualization. **Jielei Tu:** Resources, Writing - review & editing, Supervision, Data curation. **Lei Li:** Writing - review & editing. **Pinyuan Yan:** Writing - review & editing. **Weinan Zhang:** Resources, Writing - review & editing, Supervision, Data curation. **Kai Hu:** Writing - review & editing.

Acknowledgments

This work was supported by National Natural Science Foundation of China (Grant No. 61664010).

References

[1] H.K. Raut, V.A. Ganesh, A.S. Nair, S. Ramakrishna, Anti-reflective coatings: a critical, in-depth review, Energy Environ. Sci. 4 (2011) 3779–3804, https://doi.org/10.1039/c1ee01297e.
[2] A. Chabas, T. Lombardo, H. Cachier, M.H. Pertuisot, K. Oikonomou, R. Falcone, M. Verita, F. Geotti-Bianchini, Behaviour of selfcleaning glass in urban atmosphere, Build. Environ. 43 (2008) 2124–2131, https://doi.org/10.1016/j.buildenv.2007.12.008.
[3] G. Helsch, A. Mos, J. Deubener, M. Holand, Thermal resistance of nanoporous antireflective coatings on silica glass for solar tower receivers, Sol. Energy Mater. Sol. Cell. 94 (2010) 2191–2196, https://doi.org/10.1016/j.solmat.2010.07.011.
[4] G. Helsch, J. Deubener, Compatibility of antireflective coatings on glass for solar applications with photocatalytic properties, Sol. Energy 86 (2012) 831–836, https://doi.org/10.1016/j.solener.2011.12.010.
[5] T. Morimoto, Y. Sanada, H. Tomonaga, Wet chemical functional coatings for automotive glasses and cathode ray tubes, Thin Solid Films 392 (2001) 214–222, https://doi.org/10.1016/S0040-6090(01)01030-6.
[6] H. Nagel, A. Metz, R. Hezel, Porous SiO_2 films prepared by remote plasma-enhanced chemical vapour deposition – a novel antireflection coating technology for photovoltaic modules, Sol. Energy Mater. Sol. Cell. 65 (2001) 71–77, https://doi.org/10.1016/S0927-0248(00)00079-9.
[7] D. Li, F. Huang, S. Ding, Sol–gel preparation and characterization of nanoporous ZnO/SiO_2 coatings with broadband antireflection properties, Appl. Surf. Sci. 257 (2011) 9752–9756, https://doi.org/10.1016/j.apsusc.2011.05.126.
[8] R. Messner, Importance of interference in increasing metallic reflection, and its practical utilization in optics, Optik 2 (1947) 228–334.
[9] M.S.W. Vong, P.A. Sermon, Observing the breathing of silica sol-gel-derived anti-refelction optical coatings, Thin Solid Films 293 (1997) 185–195, https://doi.org/10.1016/S0040-6090(96)09041-4j.
[10] R. Prado, G. Beobide, A. Marcaide, J. Goikoetxea, A. Aranzabe, Development of multifunctional sol–gel coatings: anti-reflection coatings with enhanced self-cleaning capacity, Sol. Energy Mater. Sol. Cell. 94 (2010) 1081–1088, https://doi.org/10.1016/j.solmat.2010.02.031.
[11] K. Scheurell, E. Kemnitz, P. Garcia-Juan, J. Eicher, B. Lintner, J. Hegmann, R. Jahn, T. Hofmann, P. Löbmann, Porous MgF_2 antireflective λ/4 films prepared by sol–gel processing: comparison of synthesis approaches, J. Sol. Gel Sci. Technol. 76 (2015) 82–89, https://doi.org/10.1007/s10971-015-3754-9.
[12] D. Hu, D. Liu, J. Zhang, L. Wu, W. Li, Preparation and stability study of broadband anti-reflection coatings and application research for CdTe solar cell, Opt. Mater. 77 (2018) 132–139, https://doi.org/10.1016/j.optmat.2018.01.029.

[13] G. Dingemans, W.M.M. Kessels, Status and prospects of Al_2O_3-based surface passivation schemes for silicon solar cells, J. Vac. Sci. Technol. 30 (2012), 040802, https://doi.org/10.1116/1.4728205.

[14] D. Li, F. Huang, S. Ding, Sol–gel preparation and characterization of nanoporous ZnO/SiO_2 coatings with broadband antireflection properties, Appl. Surf. Sci. 257 (2011) 9752–9756, https://doi.org/10.1016/j.apsusc.2011.05.126.

[15] X. Sun, X. Xu, J. Tu, P. Yan, G. Song, L. Zhang, W. Zhang, Research status of antireflection film based on TiO_2, IOP Conf. Ser. Mater. Sci. Eng. 490 (2019), https://doi.org/10.1088/1757-899X/490/2/022074.

[16] S. Hao, T. Lin, S. Ning, Y. Qi, Z. Deng, Y. Wang, Research on cracking of SiO_2 nanofilms prepared by the sol-gel method, Mater. Sci. Semicond. Process. 91 (2019) 181–187, https://doi.org/10.1016/j.mssp.2018.11.022.

[17] K. Ding, X.J. Zhang, L. Ning, Z.B. Shao, P. Xiao, A. Ho-Baillie, X.H. Zhang, J.S. Jie, Hue tunable, high color saturation and high-efficiency graphene/silicon heterojunction solar cells with MgF_2/ZnS double anti-reflection layer, Nano. Energy 46 (2018) 257–265, https://doi.org/10.1016/j.nanoen.2018.02.005.

[18] K. Choi, K.J. Kim, Antireflection coating of a SiO/SiN double layer on silicon fabricated by magnetron sputtering, J. Ceram. Process. Res. 3 (2010) 341–343.

[19] T. Sertel, N.A. Sonmez, S.S. Cetin, S. Ozcelik, Influences of annealing temperature on amorphous Ta_2O_5 thin films anti-reflective performance of, Ceram. Int. 45 (2018) 11–18, https://doi.org/10.1016/j.ceramint.2018.09.237.

[20] K.X. Dong, D.J. Chen, H.F. You, Y.J. Wang, Y.Y. Zhang, X.X. Wang, Growth and characteristics of SiO_2/Si_3N_4 photonic crystal filter with anti-reflection coatings, Nnanosci. Nanotech. Let. 11 (2019) 257–265, https://doi.org/10.1166/nnl.2019.2953.

[21] Y. Yuan, X. Lu, G. Yan, R. Hong, Sol-gel preparation of antireflective coatings with abrasion resistance by base/acid double catalysis and surface treatment, Sol. Energy 155 (2017) 1366–1372, https://doi.org/10.1016/j.solener.2017.08.003.

[22] J.Y. Chen, K.W. Sun, Growth of vertically aligned ZnO nanorod arrays as antireflection layer on silicon solar cells, Sol. Energy Mater. Sol. Cell. 94 (2010) 930–934, https://doi.org/10.7567/JJAP.56.040305.

[23] J.R. Martínez, S. Palomares-Sánchez, G. Ortega-Zarzosa, F. Ruiz, Y. Chumakov, Rietveld refinement of amorphous SiO_2 prepared via sol–gel method, Mater. Lett. 60 (2006) 3526–3529, https://doi.org/10.1016/j.matlet.2006.03.044.

[24] J. Wang, J. Zhou, K. Adelihan, F. Shen, H. Li, Antireflection films based on large-area 2D hollow SiO_2 spheres monolayer opals, J. Inorg. Organomet. Polym. 29 (2018) 72–79, https://doi.org/10.1007/s10904-018-0966-9.

[25] A. Grosjean, A. Soum-Glaude, P. Neveu, L. Thomas, Comprehensive simulation and optimization of porous SiO_2 antireflective coating to improve glass solar transmittance for solar energy applications, Sol. Energy Mater. Sol. Cell. 182 (2018) 166–177, https://doi.org/10.1016/j.solmat.2018.03.040.

[26] Z. Liang, W. Li, B. Dong, Y. Sun, H. Tang, L. Zhao, S. Wang, Double-function SiO_2-DMS coating with antireflection and superhydrophobic surface, Chem. Phys. Lett. 716 (2019) 211–214, https://doi.org/10.1016/j.cplett.2018.12.030.

[27] W. Dou, P. Wang, D. Zhang, J. Yu, An efficient way to prepare hydrophobic antireflective SiO_2 film by sol–gel method, Mater. Lett. 167 (2016) 69–72, https://doi.org/10.1016/j.matlet.2015.12.146.

[28] L. Vivar Mora, A. Taylor, S. Paul, R. Dawson, C. Wang, W. Taleb, J. Owen, A. Neville, R. Barker, Impact of silica nanoparticles on the morphology and mechanical properties of sol-gel derived coatings, Surf. Coating. Technol. 342 (2018) 48–56, https://doi.org/10.1016/j.surfcoat.2018.02.080.

[29] Y. Zhu, L. Chen, C. Zhang, Z. Guan, Preparation of hydrophobic antireflective SiO_2 coating with deposition of PDMS from water-based SiO_2-PEG sol, Appl. Surf. Sci. 457 (2018) 522–528, https://doi.org/10.1016/j.apsusc.2018.06.177.

[30] R.J. Martín-Palma, L. Vázquez, P. Herrero, J.M. Martínez-Duarta, M. Schnell, S. Schaeferc, Morphological, optical and electrical characterization of antireflective porous silicon coatings for solar cells, Opt. Mater. 17 (2001) 75–78, https://doi.org/10.1016/S0925-3467(01)00022-2.

[31] P. Karasiński, J. Jaglarz, M. Reben, E. Skoczek, J. Mazur, Porous silica xerogel films as antireflective coatings – fabrication and characterization, Opt. Mater. 33 (2011), https://doi.org/10.1016/j.optmat.2011.04.003, 1989–1994.

[32] I. Barton, V. Matejec, J. Mrazek, L. Predoana, M. Zaharescu, Properties of silica and silica-titania layers fabricated from silica sols containing fumed silica, Opt. Mater. 77 (2018) 187–197, https://doi.org/10.1016/j.optmat.2018.01.037.

[33] J.Q. Xi, M.F. Schubert, J.K. Kim, E.F. Schubert, M. Chen, S.Y. Lin, W. Liu, J. A. Smart, Optical thin-film materials with low refractive index for broadband elimination of Fresnel reflection, Nat. Photon. 1 (2007) 176–179, https://doi.org/10.1038/nphoton.2007.26.

[34] K. Choi, S.H. Park, Y.M. Song, Y.T. Lee, C.K. Hwangbo, H. Yang, H.S. Lee, Nano-tailoring the surface structure for the monolithic high-performance antireflection polymer film, Adv. Mater. 22 (2010) 3713, https://doi.org/10.1002/adma.201001678.

[35] K. Pfeiffer, U. Schulz, A. Tünnermann, A. Szeghalmi, Ta_2O_5/Al_2O_3/SiO_2 - antireflective coating for non-planar optical surfaces by atomic layer deposition, in: Advanced Fabrication Technologies for Micro/Nano Optics and Photonics X, vol. 10115, 2017, pp. 1–5, https://doi.org/10.1117/12.2250272.

[36] U. Schulz, Wideband antireflection coatings by combining interference multilayers with structured top layers, Optic Express 17 (2009) 8704–8708, https://doi.org/10.1364/OE.17.008704.

[37] K. Pfeiffer, L. Ghazaryan, U. Schulz, A. Szeghalmi, Wide-angle broadband Antireflection coatings prepared by atomic layer deposition, ACS Appl. Mater. Interfaces 11 (2019), https://doi.org/10.1021/acsami.9b03125, 21887–21894.

[38] A.F. Werner Stöber, Controlled growth of monodisperse silica spheres in the micron size range, J. colloid. Interf. Sci. 26 (1968) 62–69, https://doi.org/10.1016/0021-9797(68)90272-5.

[39] L. Yan, F. qin Dong, S. Zhao, H. Yan, H. Lv, X. Yuan, Hydrophobic MgF_2 antireflective films with enhanced environmental durability by a sol–gel process, Mater. Lett. 129 (2014) 156–158, https://doi.org/10.1016/j.matlet.2014.05.036.

[40] X. Huang, Y. Yuan, S. Liu, W. Wang, R. Hong, One-step sol-gel preparation of hydrophobic antireflective SiO_2 coating on poly(methyl methacrylate) substrate, Mater. Lett. 208 (2017) 62–64, https://doi.org/10.1016/j.matlet.2017.05.028.

[41] H.S. Chen, Z.Y. Sun, J.C. Shao, Investigation on FT-IR spectroscopy for eight different sources of SiO_2, Bulletin of the Chinese Ceramic Society 30 (2011) 934–937.

[42] H.T. Hussein, U.M. Nayef, A.M.A. Hussien, Synthesis of graphene on porous silicon for vapor organic sensor by using photoluminescence, Optik 180 (2019) 61–70, https://doi.org/10.1016/j.ijleo.2018.10.222.

[43] Y. Wang, J. Wu, H. Wang, R. Chen, Effective balance of antireflection and self-cleaning properties via hollow silica nanospheres-based surface coated with scattered titania nanoparticles, Sol. Energy 122 (2015) 763–772, https://doi.org/10.1016/j.solener.2015.10.003.

[44] L. Bao, Z. Ji, H. Wang, R. Chen, Hollow rodlike MgF_2 with an ultralow refractive index for the preparation of multifunctional antireflective coatings, Langmuir 33 (2017) 6240–6247, https://doi.org/10.1021/acs.langmuir.7b00737.

[45] A. Ramizy, B.M. Salih, S.N.T. Al-Rashid, Design and optimization of silicon quantum dot antireflection coating performance for UV spectrum, Optik 152 (2018) 136–145, https://doi.org/10.1016/j.ijleo.2017.09.107.

[46] L. Bao, J. Wu, H. Wang, R. Chen, Design and preparation of broadband antireflective coatings with excellent mechanical properties, Mater. Lett. 185 (2016) 464–467, https://doi.org/10.1016/j.matlet.2016.09.070.

[47] X.X. Zhang, S. Cai, D. You, L.H. Yan, H.B. Lv, X.D. Yuan, B. Jiang, Template-free sol-gel preparation of superhydrophobic ORMOSIL films for double-wavelength broadband Antirefl ective coatings, Adv. Funct. Mater. 23 (2012) 4361–4365, https://doi.org/10.1002/adfm.201203059.

[48] S. Hao, T. Lin, S. Ning, Y. Qi, Z. Deng, Y. Wang, Research on cracking of SiO_2 nanofilms prepared by the sol-gel method, Mater. Sci. Semicond. Process. 91 (2019) 181–187, https://doi.org/10.1016/j.mssp.2018.11.022.

[49] B.T. Liu, W.D. Yeh, Antireflective surface fabricated from colloidal silica nanoparticles, Colloids Surf., A 356 (2010) 145–149, https://doi.org/10.1016/j.colsurfa.2010.01.003.

[50] Y. Wang, H.N. Wang, X.S. Meng, R.Y. Chen, Antireflective films with Si-O-P linkages from aqueous colloidal silica: preparation, formation mechanism and property, Sol. Energy Mater. Sol. Cell. 130 (2014) 71–82, https://doi.org/10.1016/j.solmat.2014.06.040.

[51] U. Mehmood, F.A. Al-Sulaiman, B.S. Yilbas, B. Salhi, S.H.A. Ahmed, M.K. Hossain, Superhydrophobic surfaces with antireflection properties for solar applications: a critical review, Sol. Energy Mater. Sol. Cell. 157 (2016) 604–623, https://doi.org/10.1016/j.solmat.2016.07.038.

[52] J.-Q. Xi, M.F. Schubert, J.K. Kim, E.F. Schubert, M. Chen, S.-Yu. Lin, W. Liu, J. A. Smart, Optical thin-film materials with low refractive index for broadband elimination of Fresnel reflection, Nat. Photon. 1 (2007) 565–567, https://doi.org/10.1038/nphoton.2007.26.

[53] W.L. Min, B. Jiang, P. Jiang, Bioinspired self-cleaning antireflection coatings, Adv. Mater. 20 (2008) 3914–3918, https://doi.org/10.1002/adma.200800791.

[54] K.C. Camargo, A.F. Michels, F.S. Rodembusch, F. Horowitz, Multi-scale structured, superhydrophobic and wide-angle, antireflective coating in the near-infrared region, Chem. Commun. 48 (2012) 4992–4994, https://doi.org/10.1039/C2CC30456B.

[55] P. Shokeen, A. Jain, V. Gupta, A. Kapoor, Multilayer silver nanoparticles embedded in graded-index dielectric layers, Opt. Mater. 66 (2017) 29–34, https://doi.org/10.1016/j.optmat.2017.01.038.